

# Method for establishing the UAV-rice vortex 3D model and extracting spatial parameters

Jiyu Li<sup>1,2</sup>, Han Wu<sup>1,2</sup>, Xiaodan Hu<sup>1,2</sup>, Gangao Fan<sup>1,2</sup>, Yifan Li<sup>4</sup>, Bo Long<sup>1,2</sup>, Xu Wei<sup>1,2</sup>, Yubin Lan<sup>2,3\*</sup>

(1. College of Engineering, South China Agricultural University, Guangzhou 510642, China;

2. National Center for International Collaboration Research on Precision Agricultural Aviation Pesticides Spraying Technology (NPAAC), Guangzhou 510642, China;

3. College of Electronic Engineering, South China Agricultural University, Guangzhou 510642, China;

4. Sunward Intelligent Equipment Co., Ltd. Changsha 410100, China)

**Abstract:** With the deepening research on the rotor wind field of UAV operation, it has become a mainstream to quantify the UAV operation effect and study the distribution law of rotor wind field via the spatial parameters of the UAV-rice interaction wind field vortex. At present, the point cloud segmentation algorithms involved in most wind field vortex spatial parameter extraction methods cannot adapt to the instantaneous changes and indistinct boundary of the vortex. As a result, there are problems such as inaccurate three-dimensional (3D) shape and boundary contour of the wind field vortex as well as large errors in the vortex's spatial parameters. To this end, this paper proposes an accurate method for establishing the UAV-rice interaction vortex 3D model and extracting vortex spatial parameters. Firstly, the original point cloud data of the wind filed vortex were collected in the image acquisition area. Secondly, DDC-UL processed the original point cloud data to develop the 3D point cloud image of the wind field vortex. Thirdly, the 3D curved surface was reconstructed and spatial parameters were then extracted. Finally, the volume parameters and top surface area parameters of the UAV-rice interaction vortex were calculated and analyzed. The results show that the error rate of the 3D model of the UAV-rice interaction wind field vortex developed by the proposed method is kept within 2%, which is at least 13 percentage points lower than that of algorithms like PointNet. The average error rates of the volume parameters and the top surface area parameters extracted by the proposed method are 1.4% and 4.12%, respectively. This method provides 3D data for studying the mechanism of rotor wind field in the crop canopy through the 3D vortex model and its spatial parameters.

**Keywords:** UAV, rice canopy, wind field, binocular vision, point cloud segmentation, spatial parameters

**DOI:** 10.33440/ijpaa.20200302.84

**Citation:** Li J Y, Wu H, Hu X D, Fan G A, Li Y F, Long B, Wei X, Lan Y B. Method for establishing the UAV-rice vortex 3D model and extracting spatial parameters. *Int J Precis Agric Aviat*, 2020; 3(2): 56–64.

## 1 Introduction

In recent years, more and more scholars at home and abroad have devoted themselves to the study of precision agriculture aviation. The intelligence and informatization of agricultural UAV has become an international trend<sup>[1-4]</sup>. As an important factor affecting agricultural UAV operations, the rotor wind field characterized by instantaneous changes has drawn wide attention<sup>[5-9]</sup>. Li Jiyu et al. studied the distribution law of the canopy wind field of the rotor UAV by integrating the wind speed parameter acquisition system and the Beidou Positioning System<sup>[10]</sup>. In 2017, Li Jiyu et al. proposed a new physical form of UAV-rice interaction vortex to represent the distribution law of rotor wind

field in the crop canopy and built an ideal matching model for it by collecting the wind speed in the vertical direction of the canopy<sup>[11]</sup>. The above research shows that when the UAV in operation, UAV-rice interaction vortex of an inverted cone shape is formed under the interaction between the rotor wind field and the rice canopy. 3D parameters of the vortex are essential for studying not only the mechanism of rotor wind field in the crop canopy but also the UAV's parameters like its working range and intensity. However, most available point cloud segmentation algorithms cannot adapt to the instantaneous changes and indistinct boundary of the vortex, which causes inaccurate 3D shape and boundary contour of the wind field vortex as well as large errors of spatial parameters.

With the development of deep learning in artificial intelligence, semantic segmentation algorithm has been widely used in 3D point cloud segmentation. Qin et al. proposed the framework of TLFnet and applied multi-view convolutional neural network (CNN) to large-scale point cloud segmentation by using airborne laser scanning for terrain scene classification<sup>[12]</sup>. Boulch et al. presented the approach of Snapnet and performed point cloud segmentation by integrating RGB-D with point cloud and utilizing the fusion strategy<sup>[13]</sup>. Zhang's research team advocated the joint task-recursive learning framework of TRL which recursively optimized the results of closed-loop semantic segmentation and monocular depth estimation through serialized task-level interaction<sup>[14]</sup>. Wu et al. introduced the framework of SqueezeSeg which transformed point cloud coordinates into tensors through two-dimensional (2D)

**Received date:** 2020-04-20 **Accepted date:** 2020-06-15

**Biographies:** **Jiyu Li**, PhD, Professor, research interests: precision agricultural aviation application, Email: 26260378@qq.com; **Han Wu**, Undergraduate student, research interests: agriculture aviation technology, Email: 15813303346@163.com; **Xiaodan Hu**, Postgraduate student, research interests: agriculture aviation technology, Email: hxdaan23@outlook.com; **Gangao Fan**, Postgraduate student, research interests: agriculture aviation technology, Email: 550052542@qq.com; **Yifan Li**, Postgraduate student, research interests: agriculture aviation technology, Email: 245576669@qq.com; **Bo Long**, Postgraduate student, research interests: agriculture aviation technology, Email: 496003608@qq.com; **Xu Wei**, Postgraduate student, research interests: agriculture aviation technology, Email: 1550710677@qq.com;

\***Corresponding author:** **Yubin Lan**, PhD, Distinguished Professor, Director, research interests: precision agricultural aviation application, Email: ylan@scau.edu.cn.

spherical projection, produced classification label of each point in conditional random field and segmented the road objects based on Multispectral LiDAR point cloud data in the process of autonomous driving<sup>[15]</sup>. The method of projection and view was utilized for point cloud segmentation in these studies and it realized 3D semantic segmentation on the basis of 2D deep learning. But in view of segmenting the UAV-rice interaction vortex, this method was not applicable because of its high precision error (over 18%) and slow segmentation speed (over 15 frames per second).

The promotion of CNN from 2D to 3D contributes to the application of the deep voxel network to point cloud segmentation. Maturana and Scherer proposed the VoxNet that fulfilled simple classification tasks through two convolutional layers, one pooling layer and two fully connected layers<sup>[16]</sup>. Chang et al. came up with a large shape library with abundant annotations called ShapeNet. ShapeNet realized data visualization of the object attributes by collecting 3D models under multiple semantic categories and providing semantic annotations for each model. Chang's study promoted data-driven geometric analysis and provided a large-scale quantitative benchmark for the exploration of computer graphics and computer vision<sup>[17]</sup>. Huang et al. introduced a 3D point cloud labeling scheme based on 3D CNN to minimize the interference of prior knowledge of the labeling<sup>[18]</sup>. Tchampi et al. advocated the framework of SEGCloud, which applied 3D fully convolutional network to point cloud segmentation by voxel, downsampling and trilinear interpolation analysis of 3D point cloud<sup>[19]</sup>. The voxel-based point cloud segmentation algorithms mentioned above fully retain the point cloud information and significantly reproduce the target features because they do not reduce dimensionality of the point cloud data, but such algorithms are so complicated in operation and demanding in storage that they are not applicable to the UAV-rice interaction vortex of instantaneous changes.

It is acknowledged that the more complex the segmentation scene is, the more accurate and robust the point cloud segmentation algorithm should be. In 2017, Charles et al. put forward a new type of depth network architecture PointNet where original point cloud data were directly input requiring no transformation. The point cloud and features were aligned via two T-net transformation networks, while features were extracted by two multilayer perceptron (MLP) and point cloud was segmented through one pooling layer. As a result, problems like point cloud original data disorder and geometric rotation were solved<sup>[20]</sup>. On the basis of PointNet, Qi et al. introduced CNN to PointNet and extracted local features by processing a group of points sampled from the metric space in a hierarchical manner so as to capture the fine geometric structures of small neighborhoods<sup>[21]</sup>. These studies concern disordered point cloud segmentation. They perform end-to-end operation without introducing other point cloud processing algorithms halfway, and reduce the complexity of point cloud segmentation algorithm. Such algorithms can extract the global features of point cloud, but they are not applicable to the UAV-rice interaction vortex that are characterized by significant boundary changes.

To cope with point cloud disorder and to reproduce features to the maximum degree, researchers have proposed segmentation algorithms based on ordered point cloud. The earliest ordered point cloud segmentation algorithm is OctNet. By using sparsity in the input data, this algorithm uses a set of unbalanced octree to divide the space into layers, puts memory allocation and computation into relevant dense regions, and develops a deeper network without affecting the resolution<sup>[22]</sup>. Klovov et al.

proposed KD-network, a feedforward neural network, which studied the parameters associated with the node weight in KD-tree by using KD-tree structure to index point cloud<sup>[23]</sup>. Su et al. advocated the SplatNet, which realized complete end-to-end processing by constructing the network structure through bilateral convolutional layer without additional data processing<sup>[24]</sup>. It is found that segmentation algorithms based on ordered point cloud feature high accuracy, solve end-to-end problems and reduce additional performance overhead. However, these algorithms cannot meet the needs of field operation because their structures are too complex and the sorting processes are time-consuming.

Nowadays, 3D point cloud segmentation algorithms are able to meet the automation requirements of emerging technologies such as the autopilot, UAV, and robot navigation. But in view of segmenting the UAV-rice interaction vortex, the application of the above-mentioned algorithms causes problems such as inaccurate 3D shape and boundary contour of the wind field vortex, and large errors in the vortex's spatial parameters. Therefore, this paper proposes a method for establishing the UAV-rice interaction wind field vortex 3D model and extracting vortex spatial parameters. This method provides 3D data for studying the mechanism of rotor wind field in the crop canopy by extracting the vortex's 3D physical parameters.

## 2 Materials and methods

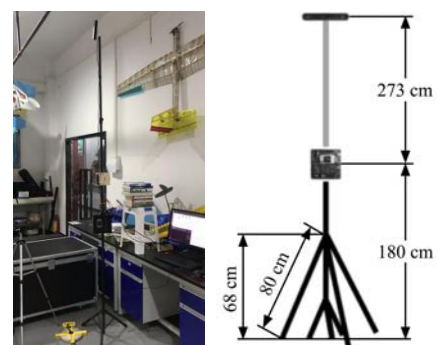
### 2.1 Materials and experiment site

This experiment was conducted in a rice research field of Guangdong Academy of Agricultural Sciences located in Zhongluotian Town, Baiyun District, Guangzhou, Guangdong, China (23°23'47.98"N, 113°26'11.79"E). At the time of the experiment, the rice was in the flowering stage and the height of rice canopy was 1.02m.

The EFT 10 kg Plant Protection UAV (Figure 1a) was utilized to simulate field spraying operation. NVIDIA® Jetson™ TX2 supercomputer module with ZED 2K Stereo Camera served as the image acquisition device (Figure 1b) to collect the left and right images of the wind field vortex generated under the interaction between rotor wind field and rice canopy.



a. UAV



b. The image acquisition device

Figure 1 Physical drawing and structure diagram of UAV and image acquisition device

## 2.2 Basic data

### 2.2.1 UAV airframe and flight parameters

The airframe and flight parameters of the EFT 10 kg Plant Protection UAV are shown in Table 1.

**Table 1 Airframe parameters and flight parameters of UAV**

Airframe parameters				Flight parameters	
Takeoff weight /kg	Main rotor diameter /m	Rotor span /m	Rotational speed /rpm	Flight height (m) distance above the canopy	Flight speed /m·s <sup>-1</sup>
15	0.75	1.2	1350	1.7-1.9	0-0.14

The EFT 10 kg Plant Protection UAV used in this experiment is medium-sized with a rotor diameter of 750 mm, a rotor span of 1.2 m and a total takeoff weight of 15 kg. The UAV hovered over the image acquisition area at the height of 1.8 m above the canopy during the experiment.

### 2.2.2 Image acquisition device

Figure 1b shows the composition of the image acquisition device and Table 2 presents its basic parameters.

**Table 2 Basic parameters of image acquisition device**

	CPU	GPU	Memory bank/spase
NVIDIA JETSON TX2 parameters	Dual core Denver 2 64-bit CPU and quad-core ARM A57 Complex	NVIDIA Pascal™ architecture with 256 NVIDIA CUDA cores	8GB LPDDR4/32 GB EMMC 5.1
ZED 2K Stereo Camera parameters	Frame rate/fps	Resolution ratio	Depth range/m
	15	4416*1242	0.2-20
Device parameters	Height of total installation/cm	Height of lifting and shrinking rod/cm	Height of the ZED stereo camera above the canopy/cm
	453	0-273	68

### 2.2.3 Experiment Parameters

In the experiment, the UAV-rice interaction vortex image acquisition device and the UAV operated as Figure 2 shows.

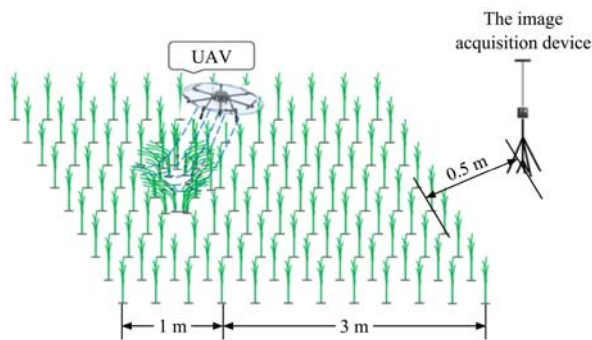


**Figure 2 UAV-rice interaction wind field vortex image acquisition experiment example**

In this experiment, the rice field ridge was 4 meter wide. To ensure the integrity of the UAV-rice interaction vortex and the accuracy of its parameters, the UAV hovered over the image acquisition area with a distance ratio of 1:3 between the UAV and the neighboring field ridge on both sides. The image acquisition device was set on the plain beside the field and 3.5 m away from the UAV. The image acquisition area was 2.5~6.5 m (D) \*~2.5~2.5 m (V) \*~4~4 m (H) (the image acquisition device as the origin).

### 2.3 Technical method

The acquisition process of the UAV-rice interaction vortex spatial parameters is illustrated in Figure 3.

Firstly, the image acquisition device collected the left and right images of the UAV-rice interaction vortex, and then the 3D point

cloud data set of the image acquisition area was obtained from the parameters of ZED 2K Stereo Camera and the depth processing algorithm. Secondly, DDC-UL point cloud segmentation algorithm was used to process the original 3D point cloud data set of the UAV-rice interaction vortex and reconstruct the 3D curved surface model. Finally, the 3D spatial parameters of the UAV-rice interaction vortex were extracted through the infinitesimal method.

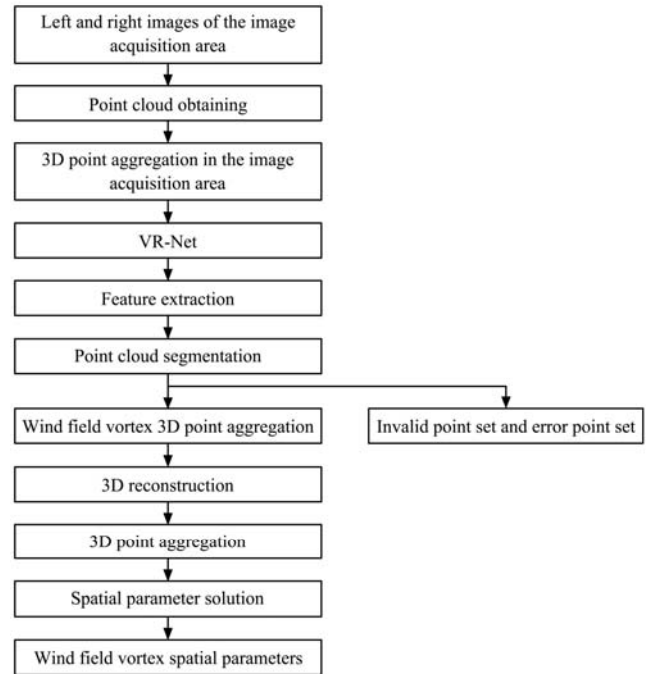


**Figure 3 Acquisition process of the UAV-rice interaction vortex spatial parameters**

### 2.3.1 Point cloud acquisition

The image acquisition device was used to collect the left and right images of the image acquisition area (Figure 4a and Figure 4b) and to match all the pixel points so as to obtain the pixel coordinate point sets corresponding to  $p_1 (X_1, Y_1)$  and  $p_2 (X_2, Y_2)$ . Assuming that the left camera of the ZED 2K Stereo Camera (marked as  $O-x_1y_1z_1$ ) was located at the origin of the world coordinate system with no rotation, the 3D point set in the image acquisition area (Figure 4c) was obtained through Function (1) based on the valid focal distance between the left and right cameras together with the rotation and translation matrix. The obtained 3D pixel point set of the image acquisition area contained not only all the points of the UAV-rice interaction vortex, but also some invalid points and wrong points with no depth information.

$$\begin{cases} x_i = z_i X_1 / F_l \\ y_i = z_i Y_1 / F_l \\ z_i = \frac{F_l (F_r t_x - X_r t_z)}{X_r (r_7 X_1 + r_8 Y_1 + F_l r_9) - F_r (r_1 X_1 + r_2 Y_1 + F_l r_3)} \end{cases} \quad (1)$$

where,  $F_l$  and  $F_r$  refer to the valid focal distance of the left and right cameras.  $x_i, y_i,$  and  $z_i$  are 3D points set in the world coordinate.  $O_1-X_1Y_1$  and  $O_r-X_rY_r$  respectively stand for the left and right camera

image coordinate system, and  $\begin{bmatrix} r_1 & r_2 & r_3 & t_x \\ r_4 & r_5 & r_6 & t_y \\ r_7 & r_8 & r_9 & t_z \end{bmatrix}$  is the rotation and

translation matrix of the ZED 2K Stereo Camera.

### 2.3.2 Point cloud segmentation

Figure 5 shows the network structure of DDC-UL point cloud segmentation algorithm.

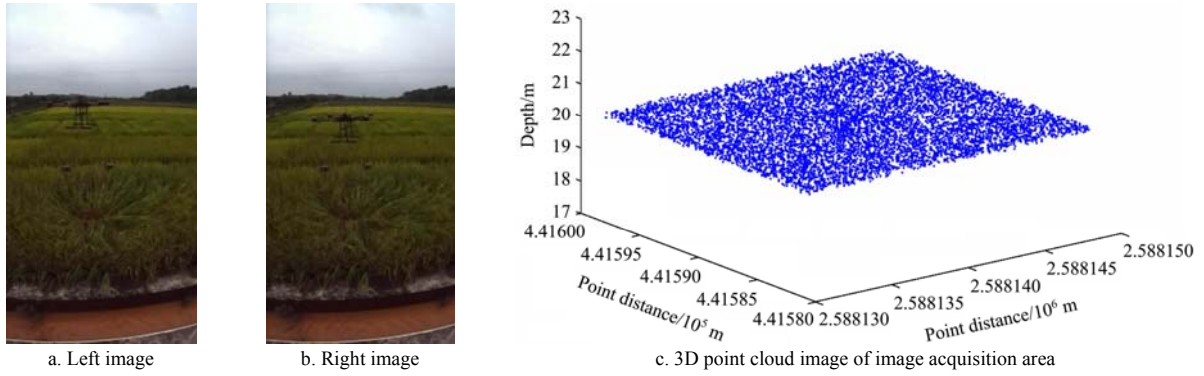


Figure 4 Left and right images of the image acquisition area and the 3D point cloud image of the image acquisition area

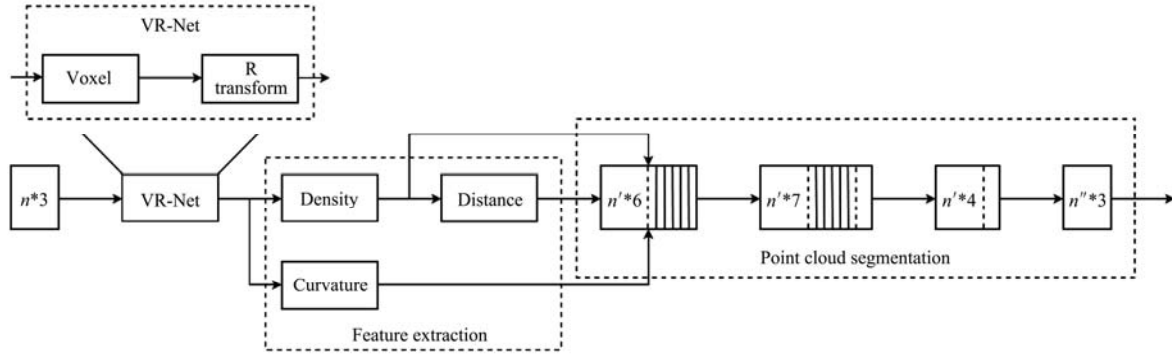


Figure 5 Network structure of DDC-UL point cloud segmentation algorithm

2.3.2.1 VR - Net transformation

In response to problems of invalid points, wrong points, and rotation error, VR-Net was introduced to the front-end of DDC-UL point cloud segmentation algorithm. The actual effect of VR-Net is shown in Figure 6. The 3D point cloud data of the image

acquisition area obtained from Section 2.3.1 were then synthesized into voxel. Voxel refers to the 3D grid of same-sized cubes in which every point is represented by its center of gravity. Then the voxel was rotated and transformed to eliminate the error caused by point cloud rotation in the process of segmentation.

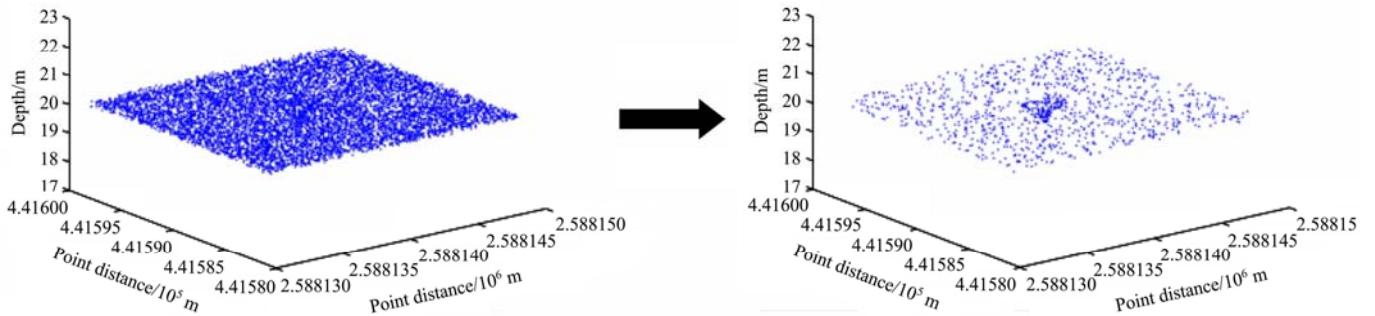


Figure 6 VR-Net transformation

2.3.2.2 Feature extraction

3D point cloud data in the image acquisition area ( $n*3$ ) were input to DDC-UL to extract the eigenvalues of density, distance, and curvature of each point in the point set.

Function (2) is the density feature solution, the core of which lies in the computation of 3D point spacing and the distance threshold.

$$\rho_i = \sum \alpha [d(i,j) - d_s] [i, j \in (1, 2, \dots, N)] \quad (2)$$

where,  $d(i,j)$  represents the point spacing and  $d_s$  stands for the distance threshold.  $\rho_i$  refers to the voxel density and  $\alpha(x)$  is the symbolic function.

Function (3) is the distance feature solution, the core of which is the solution of density feature.

$$\delta_i = \begin{cases} \max(j)[d(i, j)] \\ \min(j : \rho_i > \rho_j)[d(i, j)] \end{cases} \quad (3)$$

where,  $d(i,j)$  is the Voxel spacing and  $\rho_i$  is the Voxel density.

Function (4) is the curvature feature solution, the core of which

includes the velocity scalar, acceleration scalar, velocity vector and acceleration vector.

$$k = \sqrt{|v|^{2*} |a|^2 - (v * a)^2} / |v|^3 \quad (4)$$

where,  $|v|$ ,  $|a|$  and  $v*a$  respectively refer to the Velocity scalar, the acceleration scalar, and the velocity vector multiplied by the acceleration vector, which are obtained by differentiating the curved surface fitting function of the 3D point cloud in the image acquisition area.

2.3.2.3 Network segmentation

After feature extraction as Section 2.3.2.2 describes, each point in the 3D point set of the image acquisition area was given a 3D spatial coordinate and a 3D feature vector. The points with the largest eigenvalues in each point cluster were taken as the category points and then randomly labeled to make up different segmentation categories. The category points served as the center of each segmentation cluster, while the points in the non-central parts were sorted into its nearest category. Finally, the 3D point

set in the image acquisition area underwent feature removal through the fully connected layer, and was segmented according to categories to produce the original point cloud data of the UAV-rice interaction vortex (Figure 7).

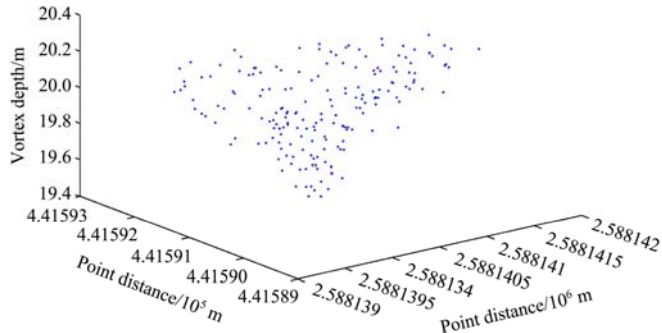


Figure 7 Original point cloud image of UAV-rice interaction vortex

2.3.3 Curved surface reconstruction

The diagram of reconstructing the point cloud curved surface

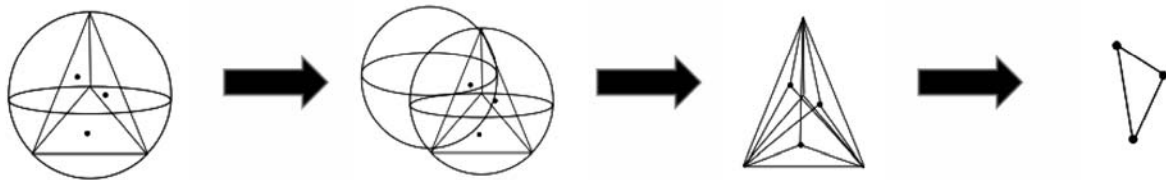


Figure 8 Point cloud surface reconstruction via Delaunay

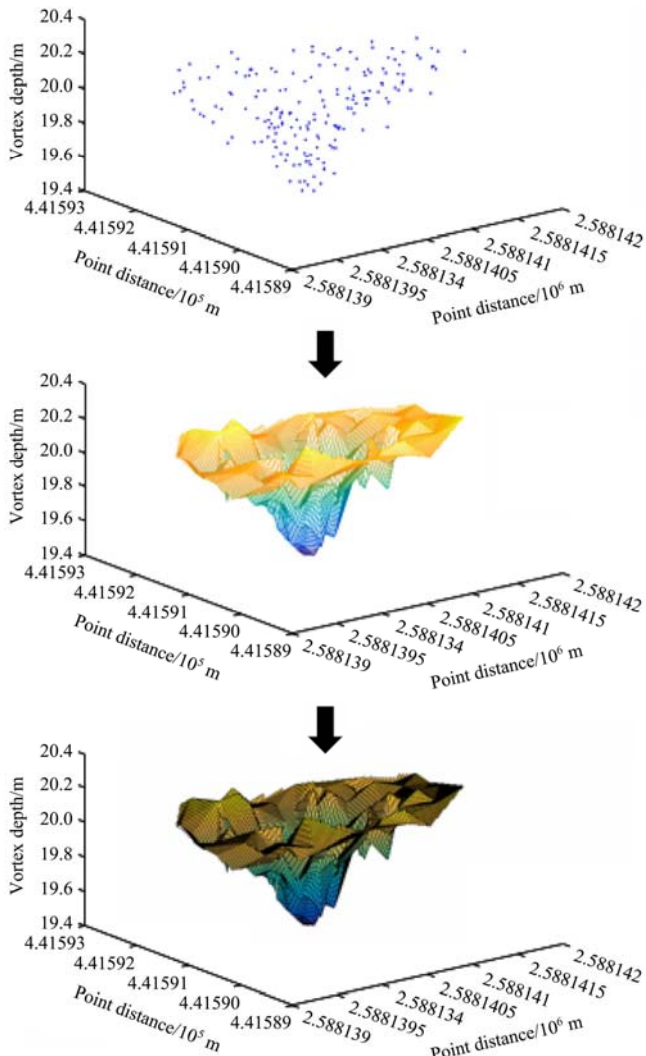


Figure 9 Reconstruction of the point cloud surface through Delaunay

by means of Delaunay is shown in Figure 8.

The original point cloud data obtained from Section 2.3.2 were placed in the 3D space, where a sufficiently large tetrahedron and its circumscribed sphere were constructed and then put into the Delaunay chain list. The tetrahedron contained all the points in the original point set of the wind field vortex. The points in the point set were then inserted into the Delaunay chain list one by one and each inserted point stuck to the following this pattern: 1) the tetrahedron whose circumscribed sphere contained the inserted point was identified; 2) the shared sides adjacent to the tetrahedron were deleted; 3) the inserted point was connected with all vertices of the tetrahedron. The above pattern was repeated until all points in the 3D wind field vortex were inserted. The initial tetrahedron was then deleted to get the 3D curve of the UAV-rice interaction vortex, from which the 3D curved surface was developed through three boundary surface.

Figure 9 presents the reconstruction of the point cloud curved surface through Delaunay.

2.3.4 Spatial parameter solution

2.3.4.1 Volume parameter solution

As shown in Figure 10, the floor of the 3D model obtained in Section 2.3.3 was divided into grids. After calculating the area of every single grid and the 3D curved surface depth in each grid, the volume of the cuboid corresponding to every grid was calculated and accumulated to get the volume parameters of UAV-rice interaction vortex. Function (5) shows the volume solution.

$$V = \sum(S_w \times D) \tag{5}$$

where,  $S_w$  is the single grid area and  $D$  refers to the 3D curved surface depth in each grid.  $S_w \times D$  represents the volume of the cuboid corresponding to every grid.

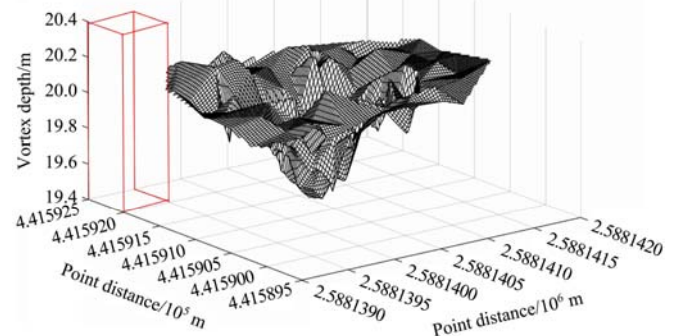


Figure 10 Schematic diagram of volume parameter calculation of UAV-rice interaction vortex

2.3.4.2 Top surface area parameter solution

As Figure 11 shows, a central point is selected on the unsealed top surface in the UAV-rice interaction vortex 3D model, and some edge points with identical angular spacing on its surface contour are also selected. The unsealed top surface is divided into sectors with different radii by the lines connecting these edge points and the center. The area of each sector is calculated and accumulated to get the area parameters of the vortex's unsealed top surface.

Function (6) illustrates the solution for the unsealed top surface area.

$$S = \sum \pi \times R_i^2 \times \frac{n^\circ}{360^\circ} \tag{6}$$

where,  $R_i$  is the radius of each sector, and  $\pi \times R_i^2 \times \frac{n^\circ}{360^\circ}$  calculates the area of each sector.

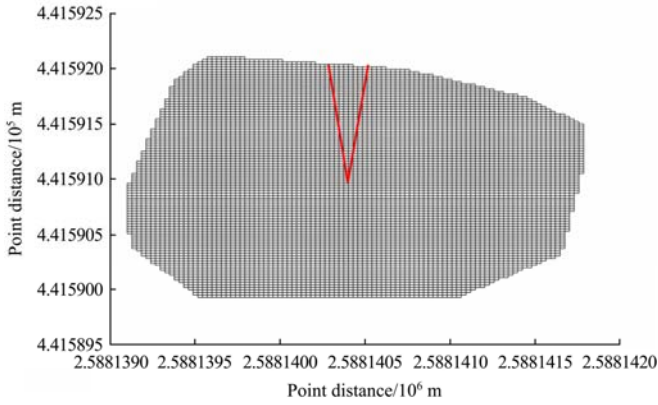


Figure 11 Schematic diagram of the calculation of the UAV-rice interaction vortex 3D model unsealed top surface

### 3 Results and discussion

In order to verify whether the method proposed in this paper could accurately establish the UAV-rice interaction wind field vortex 3D model and extract the spatial parameters, a two-level accuracy test and analysis were conducted based on the 3D point cloud data from Section 2.3.1. For level one, dynamic 3D vortex models extracted by various algorithms were compared with the static 3D vortex model extracted by the manual method. It was proved that the proposed method could best reproduce the 3D shape and boundary contour of the vortex. For level two, the dynamic vortex spatial parameters extracted by the proposed method were then compared with the static parameters extracted by

the manual method. It was confirmed that the proposed method contributed to more accurate vortex spatial parameters.

The static UAV-rice interaction vortex refers to the wind field vortex formed at the last moment of the experiment when the rice remains lodging and bending for a short period even after the UAV returns to the starting point. Although the static wind field vortex could not show the instantaneous changes of the dynamic vortex, it displayed the characteristics of the 3D shape and boundary contour of the dynamic vortex, so it could be used as the standard for analyzing the accuracy of the vortex’s 3D shape and boundary contour.

#### 3.1 Accuracy analysis of 3D shape and boundary contour of UAV-rice interaction vortex

##### 3.1.1 Result

During the experiment, the UAV hovered over the image acquisition area for 2 minutes. The original point cloud data of the image acquisition area were collected and separately processed by PointNet, Snapnet, KD-Network and DDC-UL to develop corresponding 3D models of the dynamic vortex and its three views, as they are respectively shown in Figure 12c, Figure 12d, Figure 12e, and Figure 12b. At the end of the experiment, in order to build the static vortex 3D model and capture its three views, the researcher took the Beidou Differential Positioning System into the field, and collected the feature points and boundary points of the static vortex as Figure 12a shows.

The comparison of the static results and the dynamic ones contributed to the area ratio and error rate of the three views between the manual method and various algorithms (Table 3). The accuracy of the 3D shape and boundary contour extracted by different algorithms was studied by using Function (7) to calculate the quantization area ratio.

$$P = \frac{S_{Algorithm}}{S_{Manual}} \tag{7}$$

where,  $P$  is the area quantization ratio, and  $S_{Algorithm}/S_{artificial}$  refers to the process of dividing the three views area extracted via algorithm by that extracted through manual method.

Table 3 Area quantization ratio and its error rate of each methods

Point Cloud segmentation algorithm	3D Configuration				3D error rate ( $Q_{3d}$ )	Boundary contour		
	Main view area /m <sup>2</sup>	Area quantization ratio of main view ( $P_m$ )	Left view area /m <sup>2</sup>	Area quantization ratio of left view ( $P_l$ )		Top view area /m <sup>2</sup>	Area Quantization ratio of top view ( $P_t$ )	Boundary contour error rate ( $Q_{mp}$ )
Manual extraction	0.590933	1	0.514720	1	0%	3.286531	1	0%
DDC-UL	0.606573	1.0264	0.512481	0.9956	1.540%	3.246582	0.9878	1.22%
PointNet	0.626364	1.0599	0.510026	0.9908	3.455%	2.795807	0.8506	14.94%
Snapnet	0.742321	1.2561	0.589081	1.1444	20.025%	3.888477	1.1831	18.31%
KD-Network	0.492552	0.7935	0.562203	1.1122	15.935%	2.818809	0.8576	14.24%

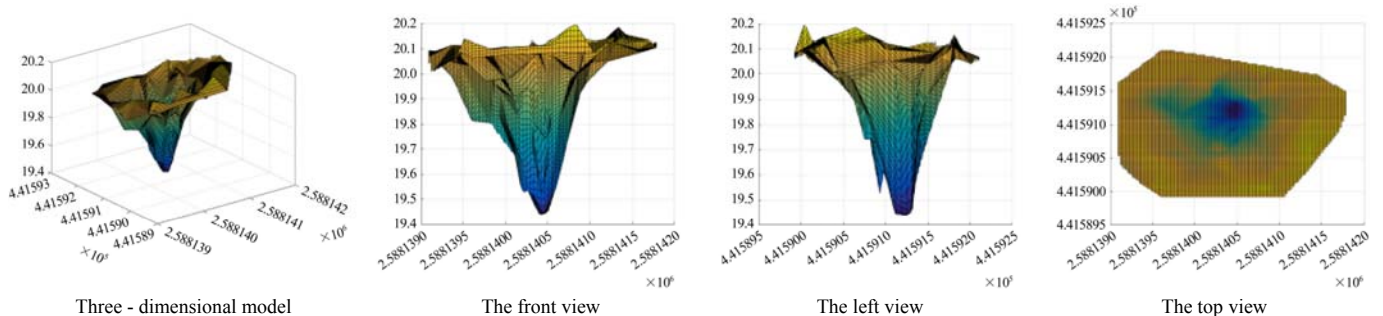


Figure 12a 3D model and three views of UAV-rice interaction vortex extracted manually

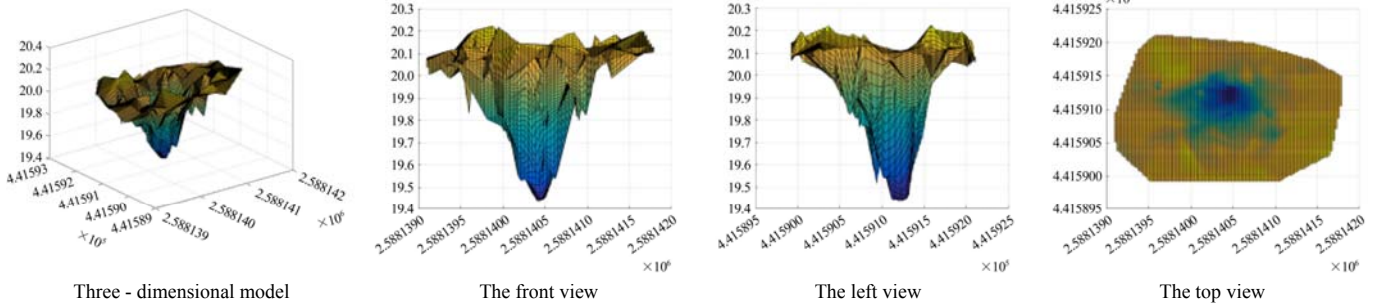


Figure 12b 3D model and three views of UAV-rice interaction vortex extracted by DDC-UL

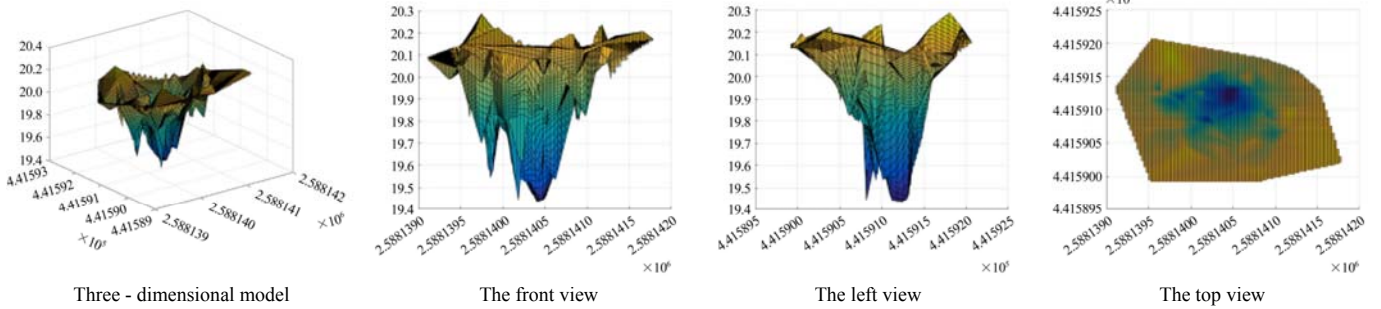


Figure 12c 3D model and three views of UAV-rice interaction vortex extracted by PointNet

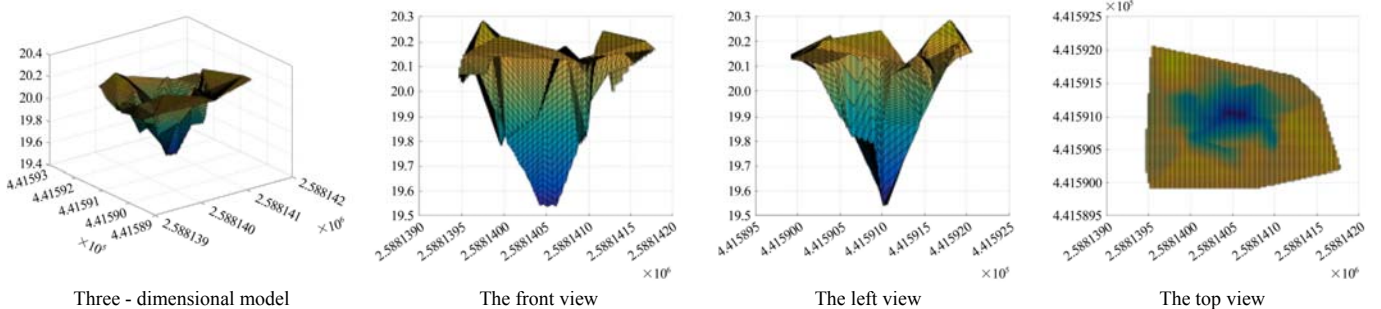


Figure 12d 3D model and three views of UAV-rice interaction vortex extracted by SnapNet

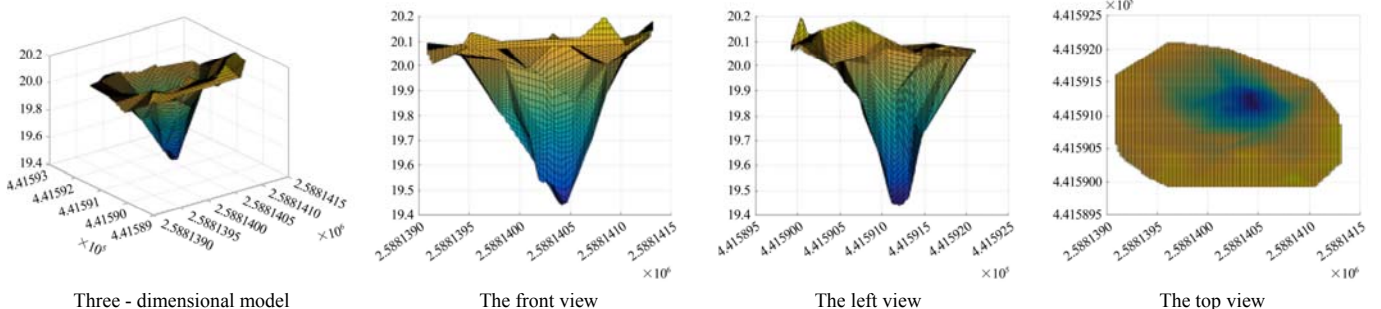


Figure 12e 3D model and three views of UAV-rice interaction vortex extracted by KD-Network

3.1.2 Data analysis

PointNet algorithm (Function (8)) integrated with T-net, MLP, and Maxpooling to extract 1024 dimensional eigenvector of the vortex point cloud, from which a 3D model of the UAV-rice interaction vortex was built. The 3D model (Figure 12c) retained the concave-convex details of its 3D curved surface with an error rate of less than 5%. However, limited by its learning capacity, PointNet was not applicable to objects with uncertain shape and indistinct features. As a result, in the process of extracting the vortex boundary, over-fitting occurred with an error rate over 14%, causing remarkable difference between the model's top contour and the actual vortex.

$$f(\{x_1, \dots, x_n\}) = g(h(x_1), \dots, h(x_n)) \quad (8)$$

where,  $f(x)$  stands for Segmentation function;  $g(h(x))$  refers to the max pooling function and  $h(x_i)$  is the feature extraction function.

Snapnet adopted Function (9) to obtain the RGB-D image of the wind field vortex and performed pixel-level marking on 2D snapshots. Different architectures were tested for the rapid back projection of tag prediction in the 3D space, and the UAV-rice interaction vortex was segmented by identifying tags. The 3D wind field vortex model (Figure 12d) could not reproduce the concave-convex details and boundary contour features of the vortex's 3D curved surface because no comparable RGB pattern was found between the inner vortex and the outer vortex. The error rate of this 3D shape was as high as 20%, while the error rate of the boundary contour reached 18.31%, indicating that the normal morphological features of the vortex has been distorted in the 3D model.

$$D = \frac{B * F}{X_R - X_T} \quad (9)$$

where,  $D$ ,  $B$ , and  $F$  represents the point cloud depth, binocular camera baseline, and binocular camera focal distance, respectively;  $X_R$  and  $X_T$  refer to left and right camera field of view.

In KD-Network, a KD tree was constructed based on the 3D point cloud of the wind field vortex, while the node feature vector  $v_i$  was calculated through Function (10) and learning parameters  $W_{di}^{li}$  and  $b_{di}^{li}$  were trained. Segmenting the features through the integration of Encoder-Decoder and Skip Connection resulted in the 3D model of UAV-rice vortex (Figure 12e). Similar to PointNet, because of its limited learning capacity and sensitiveness to interference like rotation and noise, KD-Network was not applicable to objects with unfixed shape and indistinct characteristics. Furthermore, the 3D model developed through this algorithm could not fully reproduce the 3D concave-convex details and boundary contour features with a 3D shape error and boundary contour error rate both over 14%. Therefore, this algorithm was not capable of constructing an accurate 3D model of the wind field vortex.

$$V_i = \phi(W_{di}^{li}[v_{c1(i)}; v_{c2(i)}] + b_{di}^{li}) \quad (10)$$

where,  $\phi(\cdot)$  is nonlinear element;  $W_{di}^{li}$  and  $b_{di}^{li}$  are learning parameters;  $v_{c1(i)}$  and  $v_{c2(i)}$  are child node feature vectors.

Compared with the above three point cloud segmentation algorithms, DDC-UL based itself on the global features and better presented the details of the vortex curved surface. DDC-UL's error rate of the 3D vortex shape was kept within 2%, which was 18 and 14 percentage points lower than that of Snapnet (20.025%) and the KD-Network's (15.935%). In addition, point cloud characteristics have been introduced to DDC-UL for recognition and segmentation. Therefore, being sensitive to the target object featuring instantaneous changes, DDC-UL properly adapted to the vortex boundary features. DDC-UL's error rate of boundary contour was kept at 1.22%, which was 13 percentage points lower than that of the PointNet and the KD-Network's. To sum up, with respect to the reproduction of the 3D shape and the accuracy of the boundary contour, DDC-UL outperformed the three point cloud segmentation algorithms mentioned above. The proposed method can retain the details of the vortex's curved surface and the top surface's boundary to the maximum extent, thus reproducing the overall morphology of the wind field vortex.

### 3.2 Accuracy analysis of UAV-rice interaction vortex spatial parameters

#### 3.2.1 Result

The UAV hovered over the image acquisition area for 2 minutes. Throughout the acquisition period, the UAV kept a flight speed of 0-0.14 m/s at 1.8 m above the canopy. In total, 23 frames of valid original point cloud data in the image acquisition area were collected, 20 of which were selected and processed by the proposed method to extract the spatial parameters (Table 4). After the experiment, the researcher took the Beidou Differential Positioning System into the field and collected 20 frames of feature points and boundary points in the static UAV-rice interaction wind field vortex. According to the 3D reconstruction method in Section 2.3.3 and the spatial parameter solutions in Section 2.3.4, 20 groups of static wind field vortex spatial parameters were extracted as Table 4 shows.

#### 3.2.2 Data analysis

The proposed method can extract basically accurate volume parameters of the wind field vortex. All 20 groups of volume parameters extracted by the method suggested in this paper fall into the range of 0.74m<sup>3</sup> to 0.82m<sup>3</sup>, with an average error rate of no more than 1.4%. Furthermore, F-test was conducted on the 20

groups of the volume parameters extracted by DDC-UL against those by the manual method. As Table 5 shows, the average difference is 0.010883 and the variance difference is 0.000197, while the  $F$  value (1.687662) is smaller than the critical value of 2.168252 and the  $P$  value (0.131472) is greater than 0.05. To sum up, there is no significant difference between the two sets of data.

**Table 4 Spatial parameters of the UAV-rice interaction wind field vortex**

Group	Volume/m <sup>3</sup>			Acreage/m <sup>2</sup>		
	DDC-UL	Manual Extracting	Error	DDC-UL	Manual Extracting	Error
01	0.778917	0.770733	1.06%	3.2465	3.3659	3.55%
02	0.809125	0.781954	3.47%	3.2822	3.3145	0.97%
03	0.742321	0.751221	1.18%	3.2519	3.2865	1.05%
04	0.806573	0.790244	2.07%	3.1958	3.3121	3.51%
05	0.755563	0.741269	1.94%	3.2783	3.2887	0.32%
06	0.810902	0.780488	3.90%	3.3414	3.291	1.53%
07	0.792552	0.772293	2.62%	3.2847	3.2615	0.71%
08	0.810244	0.781465	3.68%	3.2782	3.3319	1.61%
09	0.763914	0.740977	3.10%	3.3101	3.2951	0.46%
10	0.794642	0.77171	2.97%	3.3188	3.2582	1.86%
11	0.804886	0.793317	1.46%	3.2983	3.2785	0.60%
12	0.814696	0.784342	3.87%	3.2609	3.2643	0.10%
13	0.780451	0.805366	3.09%	3.3624	3.3053	1.73%
14	0.776199	0.78844	1.55%	3.281	3.3118	0.93%
15	0.769714	0.757415	1.62%	3.2484	3.3153	2.02%
16	0.792198	0.766124	3.40%	3.3367	3.2457	2.80%
17	0.80333	0.786166	2.18%	3.2626	3.2714	0.27%
18	0.750093	0.778917	3.70%	3.2573	3.2408	0.51%
19	0.794107	0.787025	0.90%	3.189	3.3279	4.17%
20	0.769039	0.772409	0.44%	3.2816	3.2711	0.32%

**Table 5 F-test between the dynamic and static vortex volume parameters**

	Variable 1	Variable 2
Average	0.785977	0.775094
Variance	0.000484	0.000287
Observed value	20	20
$d_f$	19	19
$F$	1.687662	1.687662
$P(F \leq f)$	0.131472	0.131472
$F$ Critical one-tail	2.168252	2.168252

The proposed method can extract considerably accurate top surface area parameters of the wind field vortex. The maximum difference among the 20 groups of top surface area parameters extracted by the proposed method was only 0.17m<sup>2</sup> with an average error of 4.12%. Moreover, F-test was conducted on the 20 groups of the top surface area parameters extracted by DDC-UL against those by the manual method. As Table 6 shows, the average difference is 0.01357 and the variance difference is 0.000893, while the  $F$  value (1.886481) is smaller than the critical value of 2.168252 and the  $P$  value (0.087837) is greater than 0.05. In summary, there is no significant difference between the two sets of data.

**Table 6 F-test between the dynamic and static vortex top surface area parameters**

	Variable 1	Variable 2
Average	3.278305	3.291875
Variance	0.001893	0.001003
Observed value	20	20
$d_f$	19	19
$F$	1.886481	1.886481
$P(F \leq f)$	0.087837	0.087837
$F$ Critical one-tail	2.168252	2.168252

## 4 Conclusion

This paper has proposed a method for establishing a UAV-rice interaction vortex 3D model and extracting spatial parameters. Firstly, the original point cloud data of the image acquisition area were collected. Secondly, DDC-UL processed the original point cloud data to develop the 3D point cloud image of the wind field vortex. Thirdly, 3D curved surface was reconstructed and spatial parameters were then extracted. Finally, the volume parameters and the top surface area parameters of UAV-rice interaction vortex were calculated and analyzed. This paper verifies the accuracy and authenticity of the proposed method by analyzing the experimental data which was obtained from the original image of UAV-rice interaction vortex, its 3D model and relevant spatial parameters. Conclusions are drawn as follows:

(1) The 3D model establishment method of UAV-rice interaction vortex can reproduce more than 90% of the surface details and boundary contours of vortex. The 3D model of the wind field vortex has essentially reproduced the actual vortex's morphology because it was capable of capturing the details of the vortex curved surface. The proposed method maintains the error rate of the 3D vortex shape within 2%, which is 18 and 14 percentage points lower than that of the Snapnet (20.025%) and the KD-Network's (15.935%). Moreover, the vortex's boundary contour has been properly reproduced as a result of the 3D model's adaptation to boundary variations. As for the error rate of the boundary contour, the proposed method reports 1.22% which is 13 percentage points lower than that of the PointNet and the KD-Network's.

(2) The spatial parameter extraction method of UAV-rice interaction vortex is of high accuracy and no significant difference has been found between the dynamic vortex spatial parameters and the static ones. All 20 groups of wind field vortex volume parameters are in the range of  $0.74\text{m}^3$  to  $0.82\text{m}^3$ , with an average error rate of only 1.4%. In the F-test for the 20 groups of wind field vortex volume parameters, the P value is greater than 0.05. In addition, the maximum difference among the 20 groups of wind field vortex top surface area parameters is only  $0.17\text{m}^2$ , with an average error of 4.12%. In the F-test for the 20 groups of wind field vortex top surface area parameters, the P value is also greater than 0.05.

## Acknowledgments

This research is supported by National Natural Science Foundation of China (31771682), Science and Technology Planning Project of Guangdong Province (2018A050506073), and the 111 Project (D18019). Special thanks go to the Guangdong Academy of Agricultural Sciences, to Yaoming Huang, Shuang Guo, Zhijie Liu, and Junguang Yao for helping with the field experiment.

## [References]

- [1] Lan Y B, Chen S D, Fritz B K. Current status and future trends of precision agricultural aviation technologies. *International Journal of Agricultural & Biological Engineering*, 2017; 10(3): 1–17. doi: 10.3965/j.ijabe.20171003.3088.
- [2] Zhou Z Y, Zang Y, Luo X W, et al. Technology innovation development strategy on agricultural aviation industry for plant protection in China. *Transactions of the Chinese Society of Agricultural Engineering (Transactions of the CSAE)*, 2013, 29(24): 1–10. (in Chinese)
- [3] He X K, Bonds J, Herbst A, et al. Recent development of unmanned aerial vehicle for plant protection in East Asia. *Int J Agric Biol Eng*, 2017; 10: 18–30. doi: 10.19518/j.cnki.cn11-2531/s.2017.0130.
- [4] Mogili UR, Deepak BBVL. Review on application of drone systems in precision agriculture. *Procedia Computer Science*, 2018; 133: 502–509. doi: 10.1016/j.procs.2018.07.063.
- [5] Li J Y, Zhou Z Y, Lan Y B, et al. Distribution of canopy wind field produced by rotor unmanned aerial vehicle pollination operation. *Transactions of the Chinese Society of Agricultural Engineering*, 2015; 31(03): 77–86.
- [6] Chen S D, Lan Y B, Bradley K F, et al. Effect of Wind Field below Rotor on Distribution of Aerial Spraying Droplet Deposition by Using Multi-rotor UAV. *Transactions of the Chinese Society for Agricultural Machinery*, 2017; 48(08): 105–113.
- [7] Liu J T, Wu W H, Li J, et al. Trajectory controller design for quadrotor UAVs on wind field disturbance. *Flight Dynamics*, 2016; 34(02): 47–50, 54. doi: 10.13645/j.cnki.f.d.20160110.015.
- [8] Jiang K, Wang Z H, Fan J R, et al. Droplet Deposition Rules of Multi Rotor UAV Flight Loads Impact. *Journal of Agricultural Mechanization Research*, 2020; 42(05): 25–32. doi: 10.13427/j.cnki.njyi.2020.05.004.
- [9] Zheng Y J, Yang S H, Liu X X, et al. The computational fluid dynamic modeling of downwash flow field for a six-rotor UAV. *Frontiers of Agricultural Science and Engineering*, 2018(02).
- [10] Li J Y, Zhou Z Y, Lan Y B, et al. Distribution of canopy wind field produced by rotor unmanned aerial vehicle pollination operation. *Transactions of the Chinese Society of Agricultural Engineering*, 2015; 31(3): 77–86. (in Chinese)
- [11] Li J Y, Shi Y Y, Lan Y B, et al. Vertical distribution and vortex structure of rotor wind field under the influence of rice canopy. *Computers and Electronics in Agriculture*, 2019; 159, 140–146. doi: 10.1016/j.compag.2019.02.027.
- [12] Qin N, Hu X, Dai H. Deep fusion of multi-view and multimodal representation of ALS point cloud for 3D terrain scene recognition. *ISPRS Journal of Photogrammetry and Remote Sensing*, 2018; 143: 205–212. doi: 10.1016/j.isprsjprs.2018.03.011.
- [13] Boulch A, Guerry J, Le Saux B, et al. SnapNet: 3D point cloud semantic labeling with 2D deep segmentation networks. *Computers and Graphics*, 2018; 71: 189–198. doi: 10.1016/j.cag.2017.11.010.
- [14] Zhang Z, Cui Z, Xu C, et al. Joint task-recursive learning for semantic segmentation and depth estimation. *Proceedings of European Conference on Computer Vision*, 2018. doi: 10.1007/978-3-030-01249-6\_15.
- [15] Wu B, Wan A, Yue X, et al. SqueezeSeg: Convolutional neural nets with recurrent CRF for real-time road-object segmentation from 3D lidar point cloud. *Proceedings of IEEE International Conference on Robotics and Automation*, 2018: 1887–1893.
- [16] Maturana D, Scherer S. VoxNet: A 3D convolutional neural network for real-time object recognition. *Proceedings of IEEE International Conference on Intelligent Robots and Systems*, 2015. doi: 10.1109/IROS.2015.7353481.
- [17] Chang A X, Funkhouser T, Guibas L, et al. ShapeNet: An information-rich 3D model repository. arXiv:1512.03012, 2015.
- [18] Huang J, You S. Point cloud labeling using 3D convolutional neural network. *Proceedings of International Conference on Pattern Recognition*, 2016. doi: 10.1109/ICPR.2016.7900038.
- [19] Tchapmi L, Choy C, Armeni I, et al. SEGCloud: Semantic segmentation of 3D point clouds. *Proceedings of International Conference on 3D Vision*, 2017: 537–547.
- [20] Charles R Q, Hao S, Mo K, et al. PointNet: Deep learning on point sets for 3D classification and segmentation. *Proceedings of IEEE Conference on Computer Vision and Pattern Recognition*, 2017.
- [21] Qi C R, Yi L, Su H, et al. PointNet++: Deep hierarchical feature learning on point sets in a metric space. *Advances in Neural Information Processing Systems*, 2017: 5099–5108.
- [22] Riegler G, Ulusoy A O, Geiger A. OctNet: Learning deep 3D representations at high resolutions. *Proceedings of IEEE Conference on Computer Vision and Pattern Recognition*, 2017.
- [23] Klovov R, Lempitsky V. Escape from cells: Deep KD networks for the recognition of 3D point cloud models. *Proceedings of IEEE International Conference on Computer Vision*, 2017.
- [24] Su H, Jampani V, Sun D, et al. SPLATNet: Sparse lattice networks for point cloud processing. *Proceedings of IEEE Conference on Computer Vision and Pattern Recognition*, 2018.